IEEE Access
Multidisciplinary | Rapid Review | Open Access Journal

Received May 28, 2019, accepted July 8, 2019, date of publication July 16, 2019, date of current version August 9, 2019.

Digital Object Identifier 10.1109/ACCESS.2019.2929103

Optimal Design of Saturated Switched Reluctance Machine for Low Speed Electric Vehicles by Subset Quasi-Orthogonal Algorithm

XIUPENG CUI[1], (Member, IEEE), JIANBO SUN[1], CHUN GAN[1], (Member, IEEE), CHENGLIN GU[1], AND ZHIWEI ZHANG[2]

[1]State Key Laboratory of Advanced Electromagnetic Engineering and Technology, School of Electrical and Electronic Engineering, Huazhong University of Science and Technology, Wuhan 430074, China
[2]Department of Electrical and Computer Engineering, The Ohio State University, Columbus, OH 43210, USA

Corresponding author: Jianbo Sun (jianbo.sun@hust.edu.cn)

This work was supported by the National Key Research and Development Program of China under Grant 2017YFB0102400.

ABSTRACT This paper investigates the optimal design method of switched reluctance machines (SRMs) for mitigating torque ripple and improving average torque under the low speed operation. In order to produce high torque for hill climbing or overload start-up of micro electric vehicles (EVs) and reduce the converter capacity, an SRM with four times torque overload capability and two times speed range with constant power is needed. To improve the SRM performance, first, a new method called multiphase excitation (MPE) method for calculating resultant static torque is adopted, which takes the cross-coupling and magnetic saturation into consideration to reduce the calculation error bought by the traditional method called single-phase excitation (SPE) method; second, optimal methods, including parameters sensitivity analysis, multi-objective optimization function, and winding connection types, have been taken to release the magnetic saturation, to improve average torque, and to depress torque ripple. Compared with the initial scheme, the torque ripple is minimized from 55.33% to 14.84% and the average torque is improved by 8.36%. The experimental results validate the effectiveness of the proposed methods.

INDEX TERMS Torque ripple, cross-coupling and magnetic saturation, static resultant torque, switched reluctance machine (SRM).

I. INTRODUCTION

Permanent magnet synchronous motors (PMSMs) are widely used in electric vehicles (EVs) and hybrid electric vehicles (HEVs) for its high torque density, high power density and high efficiency [1]–[3]. However, the PMSMs with rare-earth materials such as Neodymium and Dysprosium are high in cost and there is a concern about the irreversible demagnetization of permanent magnet under high temperature [4], [5]. Therefore, the electric motors with less or no rare-earth are required for the next generation of EVs and HEVs.

Several projects have been launched to investigate the substitute motors. Switched reluctance machines (SRMs), due to their merits such as simple structure, rotor robustness, working in harsh environments, higher torque overload capability at low speed, higher efficiency at high speed and so on, have been one of the possible candidates of rare-earth-free-motors for EVs or HEVs [6]–[9]. In contrast, the drawback of the torque ripple of SRMs caused by the cross-coupling and magnetic saturation when providing the peak torque is tough to avoid. Due to the high torque ripple of SRMs at low speed caused by the doubly salient structure, the switching operating principle and the saturated flux, the promotion of SRMs contrast to permanent-magnet motors in EVs is limited [10]–[12]. Therefore, it is necessary to reduce the torque ripple and enhance the minimum torque of SRMs at the same time keeping their torque density characteristics unchanged or improved. To decrease the torsional vibration of hybrid powertrain, a dynamic model is established [13], [14].

Many investigations including the motor topologies improvement and advanced control strategy have been undertaken over past few decades in order to enhance average torque and reduce torque ripple. In [15], a mutually coupled 6/4 SRM with a modified rotor pole is designed to

The associate editor coordinating the review of this manuscript and approving it for publication was Xiaosong Hu.

keep high torque density and reduce torque ripple. However, the currents of the adjacent phases holding large amplitudes simultaneously are hard to achieve at high speed for the existence of inductances. Paper [16] investigates the effects of combination of skewing stator and rotor on vibration reduction. To a certain extent, the torque ripple has been reduced, but other performance such as average torque and efficiency are also reduced at the same time, which is not an effective solution for solving torque pulsation. A novel 6/10 SRM is proposed and compared with the traditional 6/4 topology, which shows that a higher number of rotor tooth can provide lower torque ripple at non-saturation condition in [17]. However, the torque ripple could be deteriorated compared to traditional topology. Paper [18] presents a novel method of profiling the currents to minimize the torque ripple of a SRM, which is a combination of machine design and control algorithm. Instantaneous current profiling technique is adopted in a switched reluctance servo motor in [19], however, the ideal current reference profiles should be more accurate. Direct instantaneous torque and force control based on PWM control scheme is introduced to keep the torque and radial force constant, but the operating range is limited to lower speed range (up to 40∼50% of the maximum speed) [20].

A comprehensive framework for multi-objective design optimization of the SRM is proposed to synchronously achieve the target of maximizing torque density and efficiency, and minimizing the torque ripple based on design of experiments and particle swarm optimization in [21]. However, the average torque was not taken into account, which is indeed crucial for improving the torque performance. An 80 kW segmental rotor switched reluctance machine for automotive traction is optimized with static and dynamic analyses [22].

These literatures above exhibit great contribution to the average torque improve and torque ripple depress of the SRM. However, for the EVs motors with wide speed range are always connected with the gear boxes, the speed down ratio of which reaches 15, the difference between maximum and minimum torque is amplified, thus the EVs are more sensitive to the static torque ripple of SRM with four times torque overload under severe saturation. Thus, smoothing the resultant static torque waveform of the SRM under severe saturation is the key point of this paper.

In previous point of view, the phases of SRM are independent and the resultant torque can be obtained by adding the single phase torque, but under overload condition the overlapping conduction adjacent phases share the path of the stator yoke which causes the stator yoke more saturation and the cross-coupling between phases that lead to a decrease of the permeability of steel and the torque will goes down. Thus, if the saturation and the cross-coupling are ignored under overload condition, the calculation results is not true and the resultant torque is over estimated. In this paper, a new method called multiphase excitation (MPE) method is proposed to calculate the resultant static torque of the SRM under saturate condition. Compared to the traditional method called single-phase excitation (SPE) method, the MPE method takes the cross-coupling and magnetic saturation into consideration to reduce the calculation errors of the torque ripple and average torque. Then, based on the MPE method, comprehensive framework including parameters sensitivity analysis, multi-objective, multi-variable optimization function and winding connection types are proposed to mitigate the static torque ripple of the highly saturated SRM with four times torque overload. Finally, by means of the proposed optimization methods, a 12/8 SRM with four times torque over load is designed. The average resultant and torque ripple of the optimized scheme is verified by experiment results.

II. INTRODUCTION AND COMPARISON OF THE MPE METHOD AND THE SPE METHOD

When the SRMs operating at low speed with severe saturation, the back electromotive force (EMF) is low and the current can be regarded as the chopping current in the conduction interval. Thus, instead of transient magnetic field the torque waveform can be achieved by static magnetic field. There are two merits, one is that the convergences of each steps of calculation can be ensured and another is that the time consumption can be reduced. Instead of SPE method that the resultant torque is obtained by adding the torque produced by one phase excitation, the MPE method is put forward to calculate the resultant static torque of SRMs. To obtain the maximum resultant torque, the currents are set 180 electrical degrees excitation (i.e. from unaligned position to aligned position), so there will be 60 electrical degrees overlapped between phases called multiphase conduction region. With MPE method the two phases are applied current excitation simultaneously in multiphase conduction region and the resultant torque can be obtained directly without adding operation. Whereas with SPE method the resultant torque is obtained by adding the torque produced by single phase excitation. Comparing to SPE method, the saturation and cross-coupling between phases are taking into consideration in MPE method which allows accurate calculating the torque produced by multiphase excitation simultaneously.

Fig. 1 (a) and (b) show the previously designed structures of the SRM (hereafter SRM1) and the optimized one

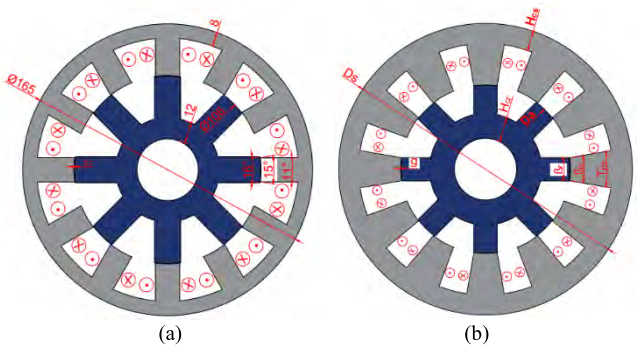

(a) (b)

FIGURE 1. Cross section of SRMs. (a) SRM1; (b) SRM2.

(hereafter SRM2), respectively. The specifications of the target SRM is shown in table 1. 180 elec. deg. conduction is employed to maximize the torque capability. With the excitation current 180A, the resultant static torques in one period of the two SRMs are shown in Fig. 2. We can see that the torque calculated by MPE method disagrees with that calculated by SPE method both in SRM1 and SRM2, during the adjacent phases conducting simultaneously (e.g. 0 elec. deg. to 60 elec. deg.) and the torque calculated by MPE method and SPE method both in SRM1 and SRM2 are the same in the single phase conduction region (e.g. 60 elec. deg. to 120 elec. deg.). This divergence is caused by cross-coupling and magnetic saturation of the adjacent phases. The influence between adjacent phases has been ignored in the point view of SPE method, however, it worsens the rock bottom of the resultant torque waveform significantly especially under saturation condition which is obvious in the SRM1 scheme. Whereas at the commutation point the torque produced by previous phase is zero, so the resultant torque produced by two phases and single phase are the same at 60 elec. deg.. Compared to SPE method, the MPE method can calculate the resultant torque more accurately, thus, in the next sections the resultant torques are calculated by MPE method.

TABLE 1. Target specifications of the SRM.

Parameters	Values
Rated voltage	72V
Rated power	4 kW
Rated torque	12.7 N·m
Efficiency	88%
Slot fill factor	0.42
Max phase current density	22A/mm^2
Phase chopping current	180A
Peak torque	51 N·m
Max speed	5800 r/min
Max power	8 kW

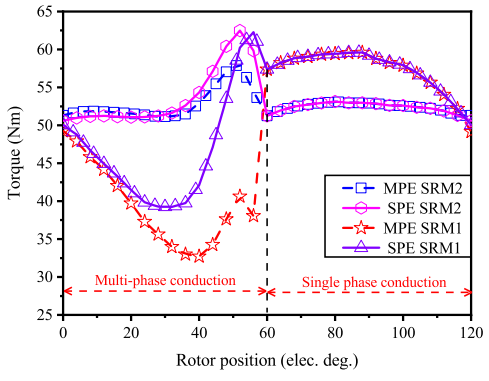

FIGURE 2. Static resultant torque in a period calculated by MPE method and SPE method respectively.

III. OPTIMIZED METHODS OF IMPROVING AVERAGE TORQUE AND MINIMIZING TORQUE RIPPLE

Due to the various geometric dimension parameters of SRMs and the nonlinear relationship between parameters and performances, the number of degrees of freedom exceed 6 and the number of calculation is over 10^6 (take 10 values at one degree of freedom), thus, it is impossible to optimize all of the parameters at the same time to obtain an excellent performance of the SRM. During the optimization process, it is found that the effects of different parameters on average and torque ripple are quite different. So parameters sensitivity analysis (PSA) is introduced to obtain the average torque and torque ripple responding to the dimension parameters. Based on the responses (i.e. sensitive or insensitive to the objectives), the multi-variable complex system is divided into several levels of subsystems. By optimizing the subsystems orderly according to the response levels, the complexity of the optimization can be reduced [23].

In the subsystems, multi-objective and multi-variable functions which combine the average torque and the torque ripple by weighted factors are adopt to obtain the optimal solutions. According to the response of sensitivity grades, the optimization sequence is from most sensitive to least sensitive and the optimized parameters are passed down in proper order. Finally, all of the geometry parameters can be confirmed. The flow chart of the proposed optimization framework is shown in Fig. 3. Firstly, define the parameter variables, constraints, and objectives of the optimization. Secondly, based on the sensitive analysis with FEA solver, divide the multi-variable complex system into several sub-system. Thirdly, perform the multi-objective optimization and obtain the optimum solutions. Then pass the optimal geometry parameters from a sub-system to the next sub-system. Finally, the optimized geometry parameters of the complex optimization of SRM can be obtained.

A. PARAMETERS SENSITIVITY ANALYSIS

To guarantee the external constraints unchanged before and after optimization, several geometric dimension parameters should be constrained. The out diameter of stator D_s and the length of the stack length L_a which are limited by the headspace for motor installation are constant. The number of turns N_p of winding that is related to the voltage and the maximum speed range and the air gap g between stator and rotor that is made as short as manufactured possible are unchanged. The current density J in windings that is limited by temperature rise in windings etc. and the slot fill percentage S_{fil} which is restricted by technics are also unchanged. The maximum chopping current is set 180A, which is determined by the capacity of converter. Besides, there are still 6 parameters including stator/rotor yoke width H_{cs}/H_{cr}, stator/rotor pole arc β_s/β_r, bottom stator tooth arc T_{ps} and rotor out diameter D_a to be optimized. The constant parameter values and the constrained variable are listed in table 2.

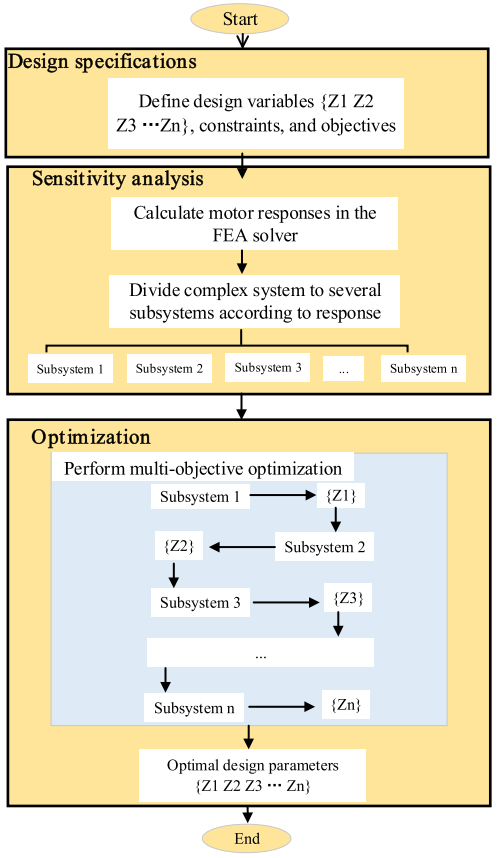

FIGURE 3. Flow chart of the proposed multi-objective optimization framework.

TABLE 2. Constant and constrained parameter values for initial and optimal design.

Parameters	unit	Initial values	Optimal values
D_s	mm	165	165
L_a	mm	125	125
N_p	-	34	34
g	mm	0.3	0.3
J	A/mm^2	22	22
S_{fil}	-	0.42	0.42
H_{cs}	mm	9.5	8~18.5
H_{cr}	mm	18	8.5~25
T_{ps}	deg	11.3	11.3~26.8
β_s	deg	15	15~20
β_r	deg	16	15~20
D_a	mm	96	92~100
Average torque	Nm	48.5	-
Torque ripple	%	55.33	-

Basic rules for the SRMs design should be followed such as:

1) The stator/rotor pole arc β_s/β_r should satisfied equation (1), for the requirement of self-start ability at any rotor position [10].

$$\begin{cases} \min\{\beta_s, \beta_r\} \geq \dfrac{2\pi}{qN_r} \\ \beta_s + \beta_r \leq \dfrac{2\pi}{N_r} \end{cases} \tag{1}$$

where q and N_r are the phase number of SRM and the number of rotor tooth.

2) To avoid the flux density unevenly distribute in magnetic circuit parts, the stator/rotor yoke width H_{cs}/H_{cr} should meet the constraints in equation (2). Here, the constraints of H_{cs}/H_{cr} are different from the literature [24], where the severely saturate condition is not considered.

$$\begin{cases} H_{cs} \geq (D_a + 2g)\sin\left(\dfrac{\beta_s}{2}\right) \\ H_{cr} \geq D_a \sin\left(\dfrac{\beta_r}{2}\right) \end{cases} \tag{2}$$

In the actual SRM, the current waveform depends on the inductances and the rotational speed. In this paper, the SRM is working at low speed, so the phase currents reach chopping value instantaneously. Thus, the current waveform can be assumed as the simple rectangular waveform to simplify the estimation of the resultant torque [25]. Fig. 4 shows the example of the current waveform. The current is simplified by a 180 elec. deg. excitation waveform and the magneto motive force (MMF) F_t is calculated as below:

$$\begin{cases} F_t = S_{fil} A_{slot} J/2 \\ A_{slot} = f\,(D_a, \beta_s, H_{cs}, \beta_{bs}) \end{cases} \tag{3}$$

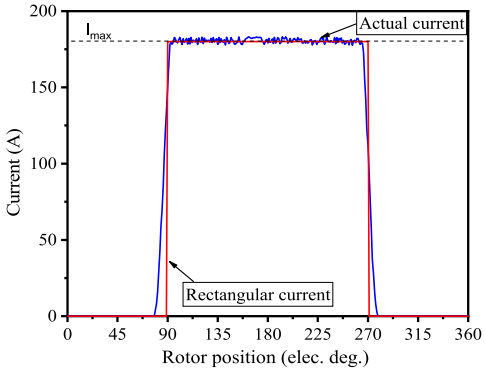

FIGURE 4. Example of the current waveform of the SRM.

where S_{fil}, A_{slot}, and J are the slot percentage, area of one stator slot, and current density. The area of one stator slot A_{slot} is a function of rotor out diameter D_a, stator pole arc β_s, stator yoke width H_{cs}, bottom stator tooth arc β_{bs}. They can be obtained refer to (4).

$$\begin{cases} H_{cs} = K_{hcs} T_s \\ T_s = (D_a/2 + g)\,\beta_s \\ \beta_{bs} = T_s/\,(D_s/2 - H_{cs}) + \Delta\beta_{bs} \end{cases} \tag{4}$$

where T_s, K_{hcs}, g, and $\Delta\beta_{bs}$ are the stator pole-width, stator yoke coefficient, air gap between stator and rotor and increment of bottom stator tooth arc.

Although new variables are in introduced, the degrees of freedom in not increased, because they are not independent. With 180 elec. deg. current excitation waveform, the period of resultant torque is 120 elec. deg. (Winding connection

types will influence the resultant torque period which will be analyzed in section IV and the analysis are based on a typical winding connection in this section). Here the resultant torque average T_{av} and torque ripple R_{ip} are expressed by the variance of static torque according to torque waveform in a period refer to (5).

$$\begin{cases} I_{av} = \dfrac{\sum_{i=1}^{n}(T_i)}{n} \\ R_{ip} = \dfrac{\max\limits_{i=1}^{n}(T_i) - \min\limits_{i=1}^{n}(T_i)}{T_{av}} \end{cases} \tag{5}$$

where n is the number of sample data in one resultant torque period, T_i is the i^{th} resultant static torque calculated by FEA among the n torque samples, $\max\limits_{i=1}^{n}(T_i)$, $\min\limits_{i=1}^{n}(T_i)$ are the maximum/minimum torque in the n torque samples.

The static resultant torque can be predicted by using the flux ψ and the current I curves and the static torque can be calculated using the flowing equations: [25]

$$\begin{cases} W_m(i,\theta) = \int_0^{\psi_{max}} id\psi = i_{max}\psi_{max} - W'_m(i,\theta) \\ W'_m(i,\theta) = \int_0^{i_{\max}} \psi di \\ T = \left.\dfrac{\partial W'_m(i,\theta)}{\partial\theta}\right|_{i=i_{\max}} \end{cases} \tag{6}$$

where $W_m(i,\theta)$ is the energy stored in a phase winding, $W'_m(i,\theta)$ is the co-energy, ψ is the flux linkage of the winding, i is the excitation current, θ is rotor position and T is the instantaneous torque. It should be note that in this model without consideration of saturation and mutual inductances, the resultant torque can expressed by (7).

$$T = \frac{1}{2}i^2\frac{\partial L}{\partial\theta} \tag{7}$$

where i and L are the phase current and self-inductance.

When it comes to multi-phase conduction, considering the mutual inductance, the flux linkage of SRM is described as below: [26]

$$\begin{bmatrix} \psi_i \\ \psi_j \\ \psi_k \end{bmatrix} = \begin{bmatrix} L_i & M_{ij} & M_{ik} \\ M_{ji} & L_j & M_{jk} \\ M_{ki} & M_{kj} & L_k \end{bmatrix} \begin{bmatrix} i_i \\ i_j \\ i_k \end{bmatrix} \tag{8}$$

where subscripts *i, j, and k* are phase *A, B,* and *C*, $\boldsymbol{L}$ and $\boldsymbol{M}$ are phase self-inductance and mutual inductance between phases, $\boldsymbol{i}$ are the phase currents. In addition, the inductance matrix is symmetrical.

The total co-energy of machine is

$$W'_m(i,\theta) = \sum_{s=1}^{n}\int_0^{i_{smax}} \psi_s di_s \tag{9}$$

where n represents the number of conducting phase simultaneously, ψ_i and i_i are the flux linkage and current of the i^{th} phase winding.

Combing (6), (7) and (9), the resultant torque can be expressed by (10) [27].

$$\begin{aligned} T = \frac{\partial W'_m(i,\theta)}{\partial\theta} &= \frac{1}{2}i_i^2\frac{\partial L_i}{\partial\theta} + \frac{1}{2}i_j^2\frac{\partial L_j}{\partial\theta} + \frac{1}{2}i_k^2\frac{\partial L_k}{\partial\theta} \\ &+ \frac{1}{2}i_i i_j\frac{\partial M_{ij}}{\partial\theta} + \frac{1}{2}i_j i_k\frac{\partial M_{jk}}{\partial\theta} + \frac{1}{2}i_k i_i\frac{\partial M_{ki}}{\partial\theta} \end{aligned} \tag{10}$$

The derivation of the resultant torque above is only suitable for liner magnetic circuit, however, with the help of frozen permeability (FP) method accounting for magnetic saturation and cross-coupling, which is increasingly used in permanent machines to calculate the on-load cogging torque and phase back EMF, the reasons of the discrepancy on resultant torques from the aspect of self-inductance and mutual-inductance can be explained. The applicability of this method is verified and the implementation steps are introduced in [28], [29]. With the FP method, the self-torque and the mutual-torque can be accurately calculated even under non-linear conditions. Therefore, equation (10) will still be applicable for resultant torque analysis even when heavy magnetic saturation occurs.

Fig. 5 shows that the response of torque average T_{av} and torque ripple R_{ip} of the six independent parameters. The Y_1 axis range (average torque) is set from 36 N·m to 52 N·m and the Y_2 axis range (torque ripple) is set from 20% to 90%. Fig. 5 (a) and (b) show that the average torque firstly increases then decreases sharply and the torque ripple goes down sharply with the increase of stator yoke coefficient K_{hcs}

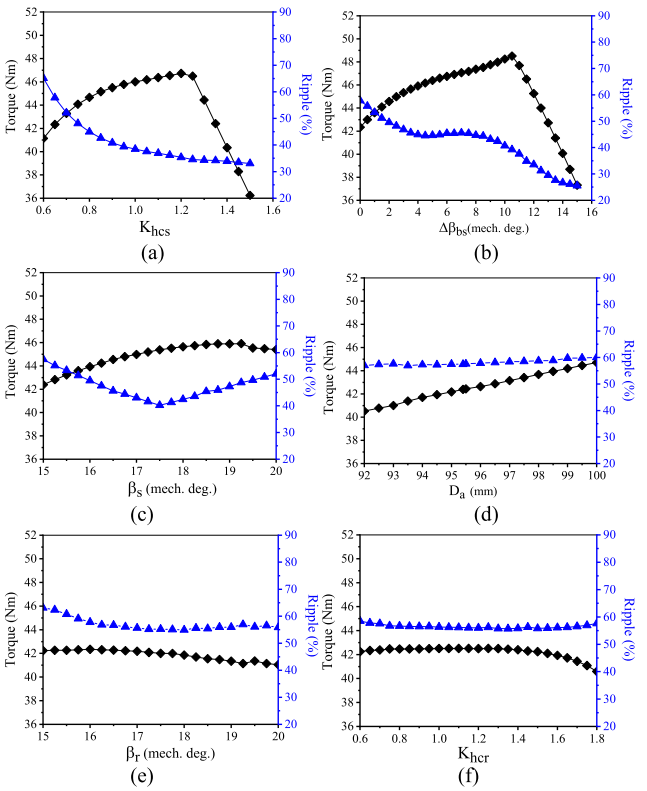

FIGURE 5. Sensitivity analysis of the geometry parameters. (a) response of K_{hcs}; (b) response of $\Delta\beta_{bs}$; (c) response of β_s; (d) response of D_a; (e) response of β_r; (f) response of K_{hcr}.

and the increment of bottom stator tooth arc $\Delta\beta_{bs}$. Evidently, the ranges caused by K_{hcs} and $\Delta\beta_{bs}$ are the maximum, thus, these two are the most sensitive parameters. Fig. 5(c) shows that the average torque is improved around 12% with the increase of stator pole arc β_s whereas the torque ripple firstly decreases then increases but still around 50%. Fig. 5(d) shows that with the increase of rotor out diameter D_a, the average torque raises gradually but torque ripple is around 60%. Thus, the average torque and torque ripple are general sensitive to D_a and β_s. Fig. 5(e) and Fig. 5(f) show that the average torque and torque ripple are constrained within relatively tight bounds with the augment of rotor pole arc β_r *and* rotor yoke coefficient K_{hcr}. So these two are the most insensitive parameters. Based on the analysis above, the parameters are divided into three grades, i.e. grades I: the most sensitivity ($\Delta\beta_{bs}$ and K_{hcs}) which should be pay more attention, grades II: general sensitivity (β_{bs} and D_a) and grades III: not sensitivity (K_{hcr} and β_r).

B. MULTI-OBJECTIVE OPTIMIZATION

According to the sensitive classification, the multi-variable complex system is divided into 3 subsystems. It is independent optimization among the three subsystems and the variables are collaborative optimization in one subsystem. Here the objective function with two weighted factors can be expressed as below,

$$\begin{cases} F(Z) = W_1\left(T^*_{av}/T_{av\_i}\right) + W_2\left(R_{ip\_i}/R^*_{ip}\right) \\ T^*_{av} = \dfrac{\left(T_{av\_\max} + T_{av\_\min}\right)}{2} \\ R^*_{ip} = \dfrac{\left(R_{ip\_\max} + R_{ip\_\min}\right)}{2} \end{cases} \tag{11}$$

where $\boldsymbol{Z} = [Z_1, Z_2]$ is the vector of variables, W_1, W_2 are the weighted factors which satisfy equation $W_1 + W_2 = 1$, T^*_{av} and R^*_{ip} are the per-unit values, T_{av_max}, T_{av_min}, R_{ip_max}, and R_{ip_min} are maximum resultant torque, minimum resultant torque, maximum torque ripple, and minimum torque ripple of all sample data, T_{av_i}, R_{ip_i} are average torque and torque ripple with certain $Z = [Z_1, Z_2]$. The optimum solution in the subsystem is determined by the objective function defined as (12).

$$F\left(Z_{opt}\right) = Min\{F(Z)\} \tag{12}$$

where $\boldsymbol{Z}_{opt}$ are the optimal values.

Fig. 6 show the response of objective function to different combinations of weighted factors for grade I, where $G1(W_1 = 0.8, W_2 = 0.2)$, $G2(W_1 = 0.5, W_2 = 0.5)$, and $G3\ (W_1 = 0.2, W_2 = 0.8)$. It can be observed that the optimal solutions of the objective function are different from each other under different combinations of weighted factors. The weighted factor represents the importance of the objective for the optimization project. So if the average torque is the focus, the W_1 can be set high, then the sample data with high average torque will be screened out; if the torque ripple is the focus, the W_2 can be set high, then the sample data with low torque

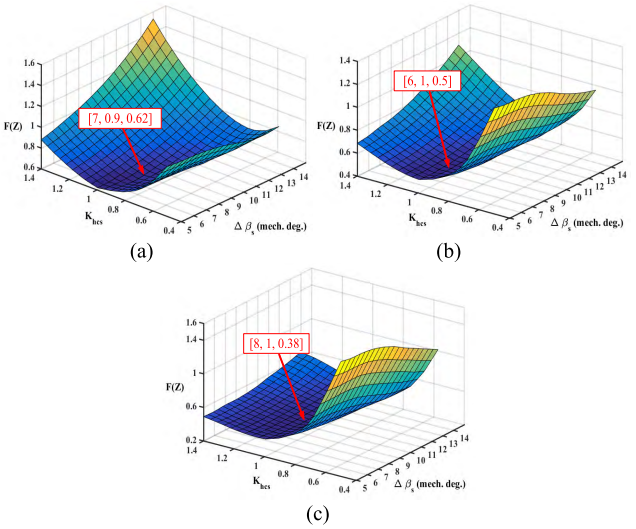

FIGURE 6. The response of objective function to different combinations of weighted factors for grade I. (a) *G1* ($W_1 = 0.8$, $W_2 = 0.2$); *G2*($W_1 = 0.5$, $W_2 = 0.5$); (c) *G3*($W_1 = 0.2$, $W_2 = 0.8$).

ripple will be screened out. Here, the average torque is the objective to be considered first, so *G1* is adopted in the grade I optimization. After optimization the values of $\Delta\beta_s$ and K_{hcs} are set 7 mechanical degrees and 0.9.

Similarly, Fig. 7 are the responses of objective function of grade II and grade III. To reach a global compromised case on average torque and torque ripple, the weighted factor variable combinations of grade II and grade III are ($W_1 = 0.8$, $W_2 = 0.2$) and ($W_1 = 0.2$, $W_2 = 0.8$), respectively. Fig. 8 (a) and (b) show the average torque and torque ripple maps of the geometric parameters. The contour and color scale indicate identical torque trajectory in the plain of K_{hcr} and β_r in vertical and horizontal axes, respectively. The maximum resultant torque is 53.6 N·m, when K_{hcr} and β_r are 1 and 19.44 mechanical degrees. Whereas the minimum torque ripple is 8.5%, when K_{hcr} and β_r are 1.6 and 15.56 mechanical degrees. Note that the values of K_{hcr} and β_r for maximum resultant torque and minimum torque ripple are not the same. Thus, the indicators are adopted to comprehensively evaluate the SRM performances. Finally, taking all of the factors into consideration, the optimized variables $\boldsymbol{Z}$ and targets average torque T_{av} and torque ripple T_{rip} are listed in Table 3. Comparing to the initial scheme as shown in Table 2, the

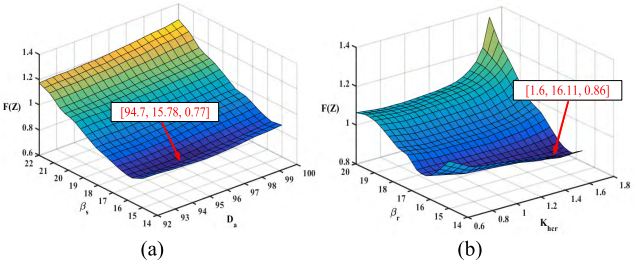

FIGURE 7. The response of objective function. (a) Grade II, ($W_1 = 0.8$, $W_2 = 0.2$). (b) Grade III, ($W_1 = 0.2$, $W_2 = 0.8$).

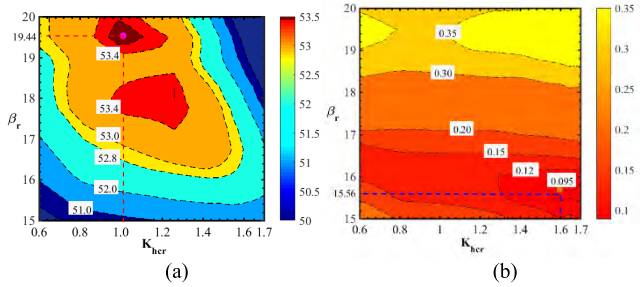

FIGURE 8. Average torque and torque ripple maps of K_{hcr} and β_r. (a) Average torque; (b) Torque ripple.

TABLE 3. Optimized parameters and targets average torque and torque ripple.

Optimal parameters						Objectives	
H_{cs} (mm)	T_{ps} (deg)	D_a (mm)	β_s (deg)	β_r (deg)	H_{cr} (mm)	T_{av} (N·m)	T_{rip} (%)
11.31	17	94.7	15.78	16.11	21.3	52.6	14.84

average torque is improved by 8.36% and the torque ripple is decreased to 14.84%. The magnetic flux density of the SRM before and after optimized are compared in Fig. 9. We can observed that the partial saturation in stator yoke has been relieved.

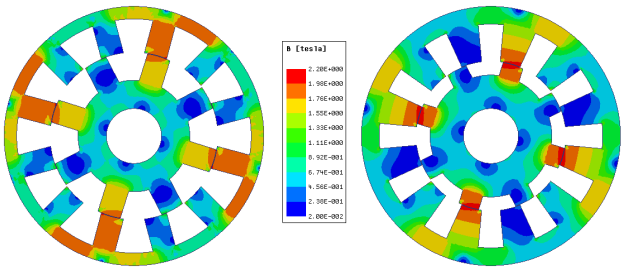

FIGURE 9. Magnetic flux density of the SRM before and after optimized. (a) Before (b) After.

IV. TOPOLOGIES OF THE WINDING CONFIGURATION

According to the stator magnetic polarity, there are three types of the winding connections in 12/8 SRM. One is NSNSNSNSNSNS (defined as Type 1), another is NNNSSSNNNSSS (defined as Type 2) and the other is NNSSNNSSNNSS (defined as Type 3, here this type is not discussed). Due to the winding polarities between adjacent phases is alternating or not, the period of the resultant torque is different, i.e., for Type 1 the period is 120 elec. deg., but for Type 2 it is 360 elec. deg. The relationship between winding connections and output torque will be discussed in this section. Using the MPE method in static magnetic field and defining the current excitation, the resultant torque in one period can be obtained by parameterizing the rotor position. If we want get the Type 2 layout from Type 1, change the polarities of middle phase as shown in Fig. 10.

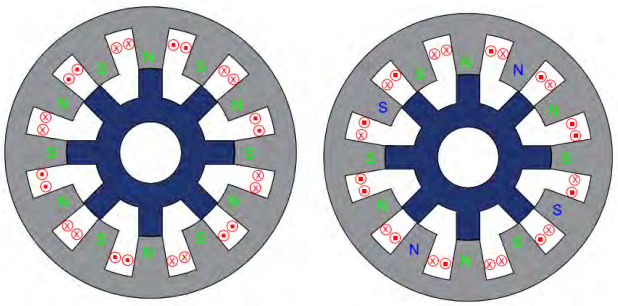

FIGURE 10. Winding connection types. (a) Type 1; (b) Type 2.

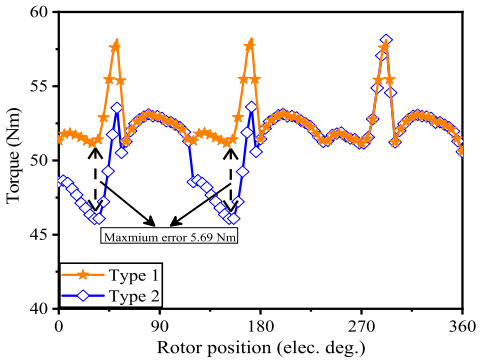

FIGURE 11. Torque waveforms of the SRM with winding connection Type 1 and Type 2.

From Fig. 11, we can observe that there is a difference between the torque waveforms of the two winding connections in the region of 0 elec. deg. to 60 elec. and 120 elec. deg. to 180 elec. deg. and the maximum difference reaches 5.69 N·m at the position of 40 and 160, elec. deg. which is caused by the torque produced by mutual inductance. The average torque decreases 1.5 N·m and the torque ripple worsens 9.0%. The Type 1 connection is used in the final scheme, for the average torque and torque ripple of Type 2 are all poor comparing to Type 1.

V. EXPERIMENT

In order to validate the theoretical analysis and perdition, the optimized 12/8 SRM prototype is built as shown in Fig. 12 and the geometric parameters of the initial and optimized are listed in Table 4.

Due to the response speed of the torque sensor in hand is not fast enough, the instantaneous resultant torque waveform cannot be obtained directly. But a test fixture as shown in Fig. 13 is designed to measure the static resultant torque with the chopping current in one cycle to prove the validity of the optimization algorithm. Comparing to the transient torque measurement method, this method overlooks the hysteresis current that is small enough comparing to the chopping current. And the torque produced by hysteresis current is a slight perturbation overlaying on the static resultant torque. Thus, the torque ripple can also be reflected by the static resultant torque at low speed at overload condition. In Fig. 13,

FIGURE 12. Stator and rotor of the optimized prototype SRM.

TABLE 4. Design parameters of the initial and optimized prototype SRM.

Parameters	unit	Initial values	Optimized values
D_s	mm	165	165
L_a	mm	125	125
N_p	-	34	34
g	mm	0.3	0.3
S_{fil}	-	22	0.42
H_{cs}	mm	0.42	11.31
H_{cr}	mm	9.5	21.3
T_{ps}	deg	18	17
T_{pr}	deg	11.3	26*
β_s	deg	15	15.78
β_r	deg	16	16.11
D_a	mm	96	94.7

T_{pr} bottom rotor tooth arc. It has little influence on average torque T_{av} and torque ripple R_{ip}, but it reduces the wind noise at high speed.

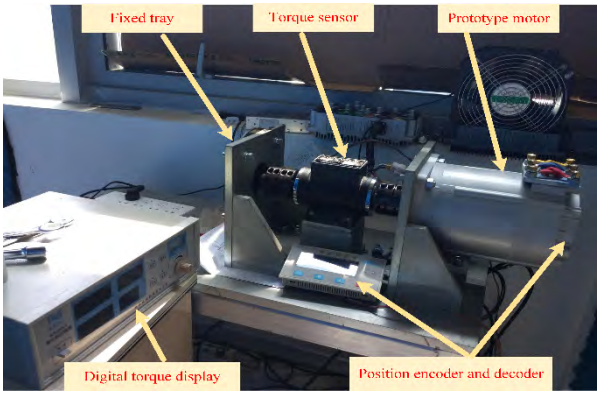

FIGURE 13. Photograph showing the implemented test rig.

the tested motor shaft, torque measuring sensor and fixed disk are connected in series by two couplings that must be hard links. The position of rotor can be obtained by the decoder and the torques can be achieved by torque sensor, the range and resolution ratio of which are 100 N·m and 0.1 N·m. The current is provided by a DC regulated power supply (model EA-PS 8240-170), whose maximum output current is 170 A, thus, the excitation current in one phase is set up 160 A in the experiment. The test steps are as follows, firstly, lock the two couplings. Second, based on the rotor position, select the phase to supply dc current and when it comes to two-phase conduction, connect two phase wires in series and the torque displayed on board is the motor static torque. Third, release the left coupling and rotate the motor shaft a certain angle according the decoder. Then, repeat the above steps.

To verify the accuracy of the experiment, the measured and calculated by FEA single phase static-torque are shown in Fig. 14. We can observe that the maximum error between calculated and measured torque is 2.42% of the maximum torque, because there are pole tips on the workmanship steel lamination of stator, which worsen the magnetic path saturation especially at the near align position. So, it should be pay more attention to the pole tips on stator tooth, if the torque ripple is a major consideration in the design.

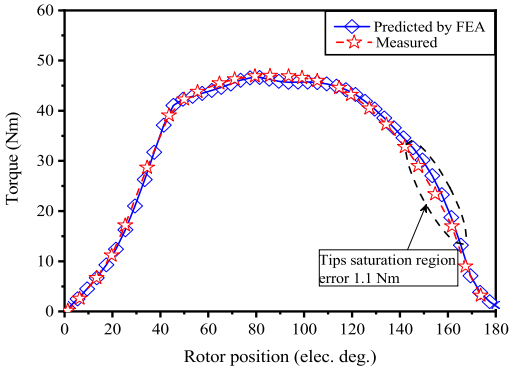

FIGURE 14. Predicted and measured single phase static-torques with dc supply 160A.

Using the workmanship steel lamination of stator with pole tips, the resultant torque waveforms are calculated with current excitation 160A. First, by adding the measured singled phase static torque (SPE method), the resultant torque is shown in Fig. 15. Meanwhile, the predicted (MPE method) and measured resultant torque waveforms of the two winding connection types are also shown in Fig. 15. We can see that the resultant torque obtained by SPE method cannot match the measured resultant torque at the multiphase conduction region, which is caused by ignoring the cross-coupling between adjacent phases and the saturation in stator yoke. Whereas, the predicted resultant torque waveforms by MPE method in the two winding types agree with the measured ones. And also the predicted and measured average torques are shown in table 5.

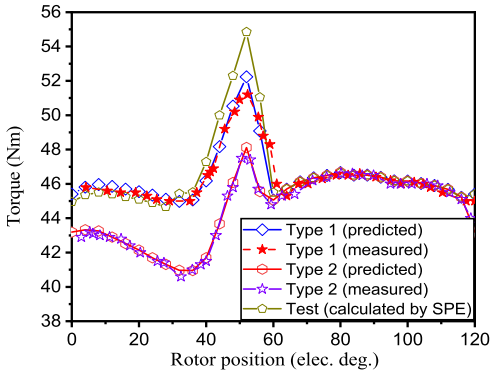

FIGURE 15. Predicted and measured resultant torques of Type1 and Type 2.

TABLE 5. Comparison of predicted and measured torque and ripple.

	Predicted		Measured	
	Average torque (N·m)	Ripple	Average torque (N·m)	Ripple (%)
Type 1	46.43	15.63%	46.8	13.3
Type 2	44.62	16.05%	45.1	15.50

To verify the response speed of the phase current at low speed at the turn-on and turn-off moment. Fig. 16 gives the current waveforms of different chopping currents at low speed 200 r/min. The turn-on is set as 0°, turn-off angle is set 22.5° and the chopping current are set as 50A, 100A, 150A and 200A, respectively. As can be seen that the current reaches the chopping current value instantaneously at turn-on and drops down zero immediately at turn-off, which verify that the excitation current can be set as chopping current at conduction region. The output torque of measured and calculated by FEA are compared in table 6. Due to the current hysteresis and back EMF, The predicted torque is a little higher than the measured one, but in an acceptable scope. The current waveform of rate power at 2800 r/min is shown in Fig. 17. The turn-on is set as −5.5°, turn-off angle is set 14°. The output torque is about 13.1 N·m, which illustrated that the optimized SRM reaches target torque.

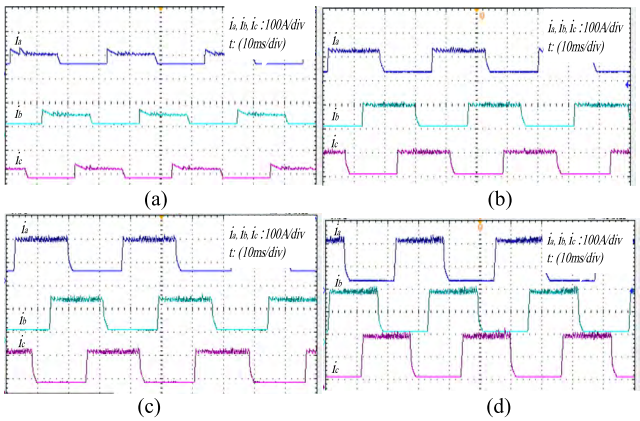

FIGURE 16. Different chopping current at 200r/min. (a) 50A, (b) 100A, (c) 150A, (d) 200A.

TABLE 6. Comparison of predicted and measured torque with different chopping current.

Chopping current (A)	Average torque measured (N·m)	Average torque predicted (N·m)	Error (%)
50	8.6	8.81	2.38
100	24.8	25.81	3.91
150	41.2	43.07	4.34
200	56.8	59.40	4.38

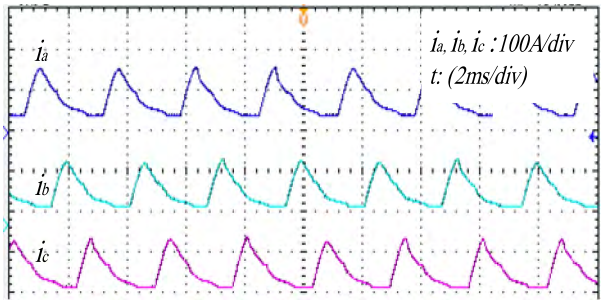

FIGURE 17. Current waveform at rated power with 2800 r/min.

VI. CONCLUSION

This paper puts forward a new method, i.e., MPE method, to calculate the resultant torque of SRMs operating at low speed, by which the influence of the multiphase overlapped conduction to saturation has been taken into consideration. Comparing to the traditional method (SPE method), the resultant torque calculated by the MPE method is closer to the measured one. Based on this method, comprehensive framework including parameters sensitivity analysis, multi-objective, multi-variable optimization function and winding connection types are investigated to mitigate the static torque ripple of the highly saturated SRM with four times torque overload. By the application of the subset quasi-orthogonal algorithm, the complexity of the SRM optimization process was reduced. In order to achieve proper compromise among average torque and torque ripple, the multi-objective optimization function with weighted factor was adopted. Finally, a 12/8 SRM with four times torque over load was designed and manufactured. The average resultant and torque ripple of the optimized SRM was verified by experimental results. Comparing the optimized SRM to the traditional one, the torque ripple is minimized from 55.33% to 14.84% and the average torque is improved by 8.36%. Measured results verified the effectiveness and practicality of the proposed methods and the optimized SRM scheme has better comprehensive performance than the initial design.

REFERENCES

[1] X. Zhu, X. Wang, C. Zhang, L. Wang, and W. Wu, "Design and analysis of a spoke-type hybrid permanent magnet motor for electric vehicles," *IEEE Trans. Magn.*, vol. 53, no. 11, Nov. 2017, Art. no. 8208604.
[2] K. Yamamoto, "The development trend of a next-generation car and the its propulsion motor," in *Proc. ICEMS*, Incheon, South Korea, Oct. 2010, pp. 25–31.
[3] I. Boldea, L. N. Tutelea, L. Parsa, and D. Dorrell, "Automotive electric propulsion systems with reduced or no permanent magnets: An overview," *IEEE Trans. Ind. Electron.*, vol. 61, no. 10, pp. 5696–5711, Oct. 2014.
[4] S. Ooi, S. Morimoto, M. Sanada, and Y. Inoue, "Performance evaluation of a high-power-density PMASynRM with ferrite magnets," *IEEE Trans. Ind. Appl.*, vol. 49, no. 3, pp. 1308–1315, May 2013.
[5] M. Takeno, A. Chiba, N. Hoshi, S. Ogasawara, M. Takemoto, and M. A. Rahman, "Test results and torque improvement of the 50-kW switched reluctance motor designed for hybrid electric vehicles," *IEEE Trans. Ind. Appl.*, vol. 48, no. 4, pp. 1327–1334, Jul. 2012.
[6] C. Gan, N. Jin, Q. Sun, W. Kong, Y. Hu, and L. M. Tolbert, "Multiport bidirectional SRM drives for solar-assisted hybrid electric bus powertrain with flexible driving and self-charging functions," *IEEE Trans. Power Electron.*, vol. 33, no. 10, pp. 8231–8245, Oct. 2018.
[7] C. Gan, J. Wu, Y. Hu, S. Yang, W. Cao, and J. M. Guerrero, "New integrated multilevel converter for switched reluctance motor drives in plug-in hybrid electric vehicles with flexible energy conversion," *IEEE Trans. Power Electron.*, vol. 32, no. 5, pp. 3754–3766, May 2017.
[8] C. Gan, Q. Sun, J. Wu, W. Kong, C. Shi, and Y. Hu, "MMC-based SRM drives with decentralized battery energy storage system for hybrid electric vehicles," *IEEE Trans. Power Electron.*, vol. 34, no. 3, pp. 2608–2621, Mar. 2019.

[9] C. Gan, Q. Sun, J. Wu, C. Shi, and Y. Hu, "A universal two-sensor current detection scheme for current control of multiphase switched reluctance motors with multiphase excitation," *IEEE Trans. Power Electron.*, vol. 34, no. 2, pp. 1526–1539, Feb. 2019.
[10] W. Uddin, T. Husain, Y. Sozer, and I. Husain, "Design methodology of a switched reluctance machine for off-road vehicle applications," *IEEE Trans. Ind. Appl.*, vol. 52, no. 3, pp. 2138–2147, May/Jun. 2016.
[11] I. Husain, "Minimization of torque ripple in SRM drives," *IEEE Trans. Ind. Electron.*, vol. 49, no. 1, pp. 28–39, Feb. 2002.
[12] M. E. Zaim, K. Dakhouche, and M. Bounekhla, "Design for torque ripple reduction of a three-phase switched-reluctance machine," *IEEE Trans. Magn.*, vol. 38, no. 2, pp. 1189–1192, Mar. 2002.
[13] X.-L. Tang, X. Hu, W. Yang, and H. Yu, "Novel torsional vibration modeling and assessment of a power-split hybrid electric vehicle equipped with a dual-mass flywheel," *IEEE Trans. Veh. Technol.*, vol. 67, no. 3, pp. 1990–2000, Mar. 2018.
[14] X. Tang, D. Zhang, T. Liu, A. Khajepour, H. Yu, and H. Wang, "Research on the energy control of a dual-motor hybrid vehicle during engine start-stop process," *Energy*, vol. 166, pp. 1181–1193, Jan. 2019.
[15] G. Li, J. Ojeda, S. Hlioui, E. Hoang, M. Lecrivain, and M. Gabsi, "Modification in rotor pole geometry of mutually coupled switched reluctance machine for torque ripple mitigating," *IEEE Trans. Magn.*, vol. 48, no. 6, pp. 2025–2034, Jun. 2012.
[16] C. Gan, J. Wu, M. Shen, S. Yang, Y. Hu, and W. Cao, "Investigation of skewing effects on the vibration reduction of three-phase switched reluctance motors," *IEEE Trans. Magn.*, vol. 51, no. 9, Sep. 2015, Art. no. 8203509.
[17] P. C. Desai, M. Krishnamurthy, N. Schofield, and A. Emadi, "Novel switched reluctance machine configuration with higher number of rotor poles than stator poles: Concept to implementation," *IEEE Trans. Ind. Electron.*, vol. 57, no. 2, pp. 649–659, Feb. 2010.
[18] R. Mikail, I. Husain, M. S. Islam, Y. Sozer, and T. Sebastian, "Four-quadrant torque ripple minimization of switched reluctance machine through current profiling with mitigation of rotor eccentricity problem and sensor errors," *IEEE Trans. Ind. Appl.*, vol. 51, no. 3, pp. 2097–2104, May/Jun. 2015.
[19] H. Makino, S. Nagata, T. Kosaka, and N. Matsui, "Instantaneous current profiling control for minimizing torque ripple in switched reluctance servo motor," in *Proc. IEEE ECCE*, Montreal, QC, Canada, Sep. 2015, pp. 3941–3948.
[20] A. Klein-Hessling, A. Hofmann, and R. W. De Doncker, "Direct instantaneous torque and force control: A control approach for switched reluctance machines," *IET Electr. Power Appl.*, vol. 11, no. 5, pp. 935–943, May 2017.
[21] C. Ma and L. Qu, "Multiobjective optimization of switched reluctance motors based on design of experiments and particle swarm optimization," *IEEE Trans. Energy Convers.*, vol. 30, no. 3, pp. 1144–1153, Sep. 2015.
[22] J. D. Widmer, R. Martin, and B. C. Mecrow, "Optimization of an 80-kW segmental rotor switched reluctance machine for automotive traction," *IEEE Trans. Ind. Appl.*, vol. 51, no. 4, pp. 2990–2999, Jul./Aug. 2015.
[23] S. Song, L. Ge, H. Liu, and W. Liu, "Design and multi-objective optimization method of switched reluctance machines," *Trans. China Electrotech. Soc.*, vol. 29, no. 5, pp. 197–204, May 2014.
[24] Y. Zhu, W. Wei, C. Yang, and Y. Zhang, "Multi-objective optimisation design of two-phase excitation switched reluctance motor for electric vehicles," *IET Electr. Power Appl.*, vol. 12, no. 7, pp. 929–937, Aug. 2018.
[25] K. Kiyota, S. Nakano, and A. Chiba, "A fast calculation method of optimal ratio of outer diameter and axial length for torque improvement in switched reluctance motor," *IEEE Trans. Ind. Appl.*, vol. 54, no. 6, pp. 5802–5811, Nov./Dec. 2018.
[26] W. Ding, Y. Liu, and Y. Hu, "Performance evaluation of a fault-tolerant decoupled dual-channel switched reluctance motor drive under open-circuits," *IET Electric Power Appl.*, vol. 8, no. 4, pp. 117–130, Apr. 2014.
[27] W. Ding, L. Liu, J. Lou, and Y. Liu, "Comparative studies on mutually coupled dual-channel switched reluctance machines with different winding connections," *IEEE Trans. Magn.*, vol. 49, no. 11, pp. 5574–5589, Nov. 2013.
[28] G. J. Li, Z. Q. Zhu, X. Y. Ma, and G. W. Jewell, "Comparative study of torque production in conventional and mutually coupled SRMs using frozen permeability," *IEEE Trans. Magn.*, vol. 52, no. 6, Jun. 2016, Art. no. 8103509.
[29] X. Cui, J. Sun, and C. Gu, "Comparative study of performance for different winding connections of dual-channel switched reluctance machine using frozen permeability," in *Proc. IEEE 4th SPEC*, Singapore, Dec. 2018, pp. 1–6.

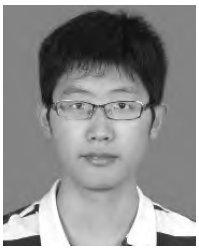

XIUPENG CUI (M'17) received the B.S. degree in applied physics from the Shenyang University of Technology, Shenyang, China, in 2014. He is currently pursuing the Ph.D. degree with the School of Electrical and Electronic Engineering, Huazhong University of Science and Technology, Wuhan, China.

His research interests include switched reluctance motor design and control, particularly for the optimization of low motor torque ripple, and high efficiency synchronous reluctance motor design and control.

JIANBO SUN received the B.S. and Ph.D. degrees from the Huazhong University of Science and Technology, Wuhan, China, in 1998 and 2005, respectively, where he is currently an Associate Professor with the School of Electrical and Electronic Engineering.

He has published over 30 technical papers in leading journals and conference proceedings. His research interests include high-speed and high-power motors' design, and starter/generator all-in one motor design and control.

CHUN GAN (M'14) received the Ph.D. degree in electrical engineering and motor drives from Zhejiang University, Hangzhou, China, in 2016.

From 2016 to 2018, he was a Research Associate with the Department of Electrical Engineering and Computer Science, University of Tennessee, Knoxville, TN, USA. He is currently a Professor with the School of Electrical and Electronic Engineering, Huazhong University of Science and Technology, Wuhan, China. He has authored/coauthored more than 60 peer-reviewed technical papers, including more than 35 IEEE Transaction papers. He holds 12 issued/published invention patents. His research interests include electrical motor drives, electrical motor design, electric vehicles, hybrid vehicles, and high-efficiency power converters.

Dr. Gan was a recipient of the 2018 Highlighted Paper Award from the IEEE TPEL, the 2018 Marie Sklodowska-Curie Actions Seal of Excellence Award from European Commission, the 2016 Excellent Ph.D. Graduate Award, and the 2015 Top Ten Excellent Scholar Award in Zhejiang University.

CHENGLIN GU was born in Shangrao, Jiangxi, China, in 1954. He received the Ph.D. degree from the Huazhong University of Science and Technology, Wuhan, China, in 1989, where he is currently a Professor with the School of Electrical and Electronic Engineering.

He has been a Visiting Professor with the Manchester University of Technology (UMIST), U.K., since 1995. His research interests include new type of electric machines and drives, including synchronous reluctance motor and permanent magnet machines for electric vehicle applications.

Dr. Gu was a Founding Member of the International Society of Computational Magnetism (ICS) and a member of the Chinese Society of Electronics.

ZHIWEI ZHANG received the Ph.D. degree in electrical engineering from the Huazhong University of Science and Technology, Wuhan, China, in 2016.

He is currently a Visiting Scholar with the Department of Electrical and Computer Engineering, The Ohio State University, Columbus, OH, USA. His major research interests include the design and analysis of high-performance electric machines, variable-speed AC drives, and transportation electrification.